Compressive Sensing Techniques for Rapid Production Test and Diagnostics of Electrically Large Nose-Mounted Commercial Radomes

Stuart F. Gregson[1,2], FELLOW, AMTA, and Clive G. Parini[2]
(1) NEXT PHASE MEASUREMENTS (NPM), GARDEN GROVE, CALIFORNIA, U.S.
(2) QUEEN MARY UNIVERSITY OF LONDON, LONDON, U.K.

***Abstract*—A new sparse sampling and compressive sensing based reconstruction and near-field imaging technique is introduced for the measurement of electrically large production test and diagnostics of nose-mounted commercial radomes. Simulated results are presented, where it is demonstrated that far-field results with an equivalent multipath level of better than -60dB can be obtained from circa 10% of the points required by a classical Nyquist equi-angular spherical near-field acquisition scheme for the case of an electrically large, *i.e.* full size, commercial airliner nose-mounted radome enclosing an x-band weather radar. Furthermore, a new method for the rapid noninvasive nondestructive imaging and identification of defects within these radomes is presented that provides significantly clearer fault detection at a far earlier stage within the radome measurement campaign than has previously been possible.**

Index Terms*— *commercial radome measurements, compressive sensing, diagnostics, imaging, robotic test system, sparse sampling, spherical near-field.

I. INTRODUCTION

The recent trend towards constructing antenna measurement ranges employing multi-axis industrial robotic positioners is becoming ever more widespread [1, 2, 3, 4, 5]. This new generation of test systems provides a near limitless degree of flexibility in terms of measurement types and scan geometries admitting possibilities that go far beyond the capabilities of classical antenna measurement systems and can even deliver measurement types not conceived at the time the facility was originally installed. One recent example involves the use of a dual robotic antenna measurement system for the near-field test and measurement of commercial aircraft nose-mounted radomes [6, 7]. These measurements typically involve extended measurement times due to the need to acquire two-dimensional near-field data to obtain the requisite asymptotic far-fields. This paper introduces a new approach for the production test, verification, and imaging of commercial aircraft nose-mounted radomes that uses a total difference based, sparse sampling technique that aims to drastically reduce the amount of near-field data required and thereby also shortening measurement times [7].

Over recent years, Sparse Sampling (SS) and Compressive Sensing (CS) based techniques have been deployed successfully in a variety of free-field antenna measurement applications which have included radar imaging [8], cylindrical [9] and spherical near-field measurements [10], far-field reflection suppression [11], as well as for array antenna measurements and diagnostics [12, 13]. Many of these applications rely on the inherent sparsity of the associated modal bases [14]. However, that is not necessarily sufficient in all cases and thus recourse to total-difference based techniques, analogous to that which is employed by Magnetic Resonance Imaging (MRI) scanners can become unavoidable [15]. Recently, this approach has been successfully applied to the SNF case, where it was demonstrated that it could be effectively used to characterize electrically large, electronically scanned, active array antennas using SNF data employing an equivalent current (EC) based algorithm [15]. A detailed treatment of the total-difference, EC based, CS method for the planar and spherical geometries can be found presented in the open literature, *e.g.* [14]. More recently [7], this approach was adapted to enable the technique to be used to accommodate scale model, nose mounted, radomes. In this paper, for the first time, that work has been extended and is applied to full size test articles where here, a Boeing 737 nose-mounted, commercial, radome is taken as an example test case. This imposes very specific demands in terms of machine resources and processing times with this point being expounded below.

In Figure 1 we present a picture of a commercial nose-mounted radome installed around a circular aperture linearly polarised slotted waveguide array weather radar antenna that is installed on an industrial 6-axis collaborative robot (CoBot). In turn, the CoBot is mounted on an azimuth stage which is used as the ϕ-axis of a conventional spherical near-field (SNF) measurement system. Here, the z-axis of the spherical system is aligned vertically with the local gravity vector. Shown to the left of the radome in Figure 1 is a 6-axis industrial robot which provide the synthesised θ-scanning axis which is of an over-head scanning arm type arrangement. Together, these form the spherical scanning axes which allow the acquisition of standard SNF data in a form that is automatically amenable for processing using any standard spherical near-field to far-field transformation algorithm, *cf.* [14]. Figure 2 contains a mechanical drawing showing an exploded view of the slotted waveguide weather radar antenna installed on a 6-axis CoBot which is being used to emulate a conventional antenna gimbal [14, 6]. This is installed behind the nose-mounted commercial radome which itself is attached to the floor-mounted ϕ-axis azimuth stage. More information on the other uses of this novel, flexible, antenna measurement system can be found in the open literature, *e.g.* [1] and which include planar and spherical near-

field measurement geometries, far-field measurements, and three-antenna extrapolated gain and polarisation measurements.

Through their standards documents [16, 17, 18], the Radio Technical Commission for Aeronautics (RTCA) prescribe and control the test and measurement requirements for nose-mounted commercial aircraft radomes with DO-213A in particular specifying the minimum operational performance standard for these radomes which admits the use of near-field measurement techniques within the evaluation process. However, the large number of prescribed mechanical pointing angles at which the weather radar is required to be positioned during the radome measurement campaign means that total test times can be somewhat extensive, rendering any technique capable of providing faster acquisitions and reduced test times extremely desirable.

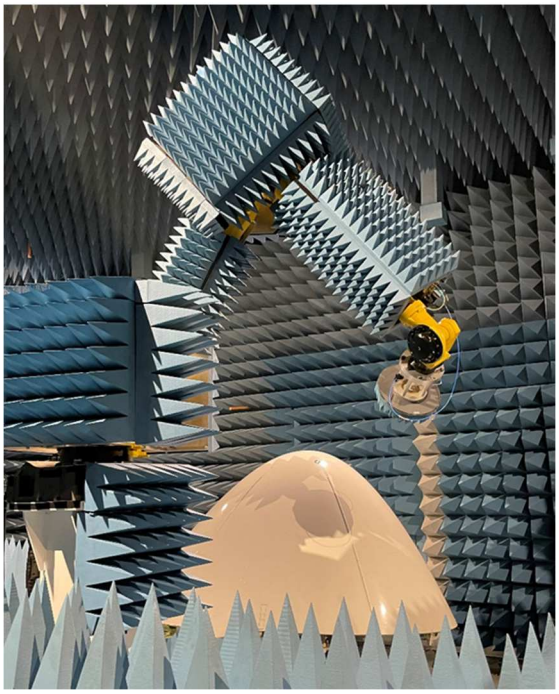

Figure 1: Picture of a new robotic antenna measurement system for commercial nose-mounted radome measurements, courtesy of Boeing.

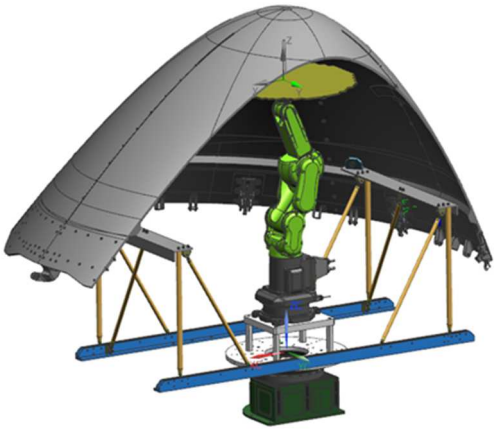

Figure 2: Picture of weather radar antenna installed on 6-axis CoBot placed behind a nose-mounted commercial radome.

II. Overview of SS & CS Radome Processing

A detailed development of the total-difference (TD), EC based, CS method for the spherical near-field measurement case can be found presented within the open literature, *e.g.* [7, 12, 13, 15], and, because of space constraints it is not repeated here with only a summary overview being provided. In principle, we exploit the fact that our application lies within a production test environment where we can assume the presence of a reference 'gold' radome to undertake a discretised back propagation from the spherical near-field measurement of the *difference* between the measurement of the, assumed defective, production radome, and the assumed ideal 'gold' reference radome. Adhering to the restricted isometry property (RIP) [12], this is accomplished using a small ensemble of, randomly located, spherical near-field measurements. Here, the intention is to minimise the number of measurement points, M, required to accurately and reliably measure the production unit in the NF, whilst accurately reconstructing the weather radars far-field pattern. Merely reducing the number of measurement points by itself is not sufficient to guarantee a reduction in overall test times, we can assume that a suitable measurement trajectory can be found through the point that, providing the reduction is significant, can be relied upon to reduce total test times [19]. Here, we are attempting to reconstruct a discrete set of magnetic surface currents that are located across the non-canonical exterior surface of the radome under test. This provides additional valuable information concerning the health of the assumed defective production test radome. Although in principle, it might be possible to examine the excitations of the array antenna, or perhaps the spherical mode coefficients (SMC) of the measurement as a whole, as it is the radome itself that is under investigation, and is that which is assumed to be changing by virtue of being defective, neither of these traditional domains are in fact sparse. The array excitations are not spare because of spatial diffraction, and the SMCs are no sparse by virtue of the large electrical size of the problem. Therefore, these factors greatly limit the probability of success of CS and SS based reconstruction algorithms [7].

Figure 3 contains an overview of the data processing used in this study. Here, we start by using a model of a linearly polarised slotted waveguide array antenna which is installed behind an "ideal" radome. We next compute the fields illuminating the radome prior to propagating those fields to a spherical near-field acquisition surface. In this way, it is possible to perturb those fields on the radome surface in amplitude and phase to emulate a defective radome and thereby obtain two different SNF measurements that can be used to validate the new EC based CS processing. We compute the "total difference" field from these two simulated measurements before back propagating to the non-canonical radome surface which is taken to be the sparce domain. This back propagation is accomplished using the EC based CS processing developed in [13, 15]. A variety of different solver implementations can be used to accomplish the basis pursuit (BP) task with SPGL1 [20], YALL1 [22] being commonly used algorithms. This allows us to determine the true fields for the defective radome and allow the visualisation of any defects before computing the corresponding complete, *i.e.* non-sparse, spherical near-fields. These spherical near-fields can then be transformed to the far-field using any standard probe

corrected spherical near-field to far-field transformation algorithm [14].

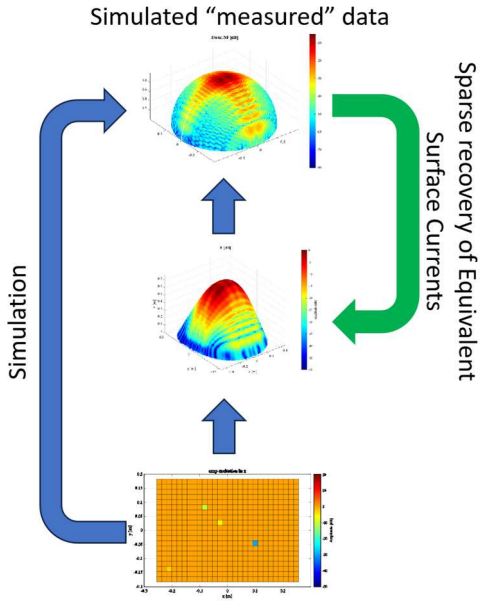

Figure 3: Schematic representation of the data processing chain utilizing the compressive sensing the recover the equivalent surface currents.

III. CS Reconstruction of Full Boeing 737 Radome

For the case of the full Boeing 737 radome, a SNF measurement radius of 1.38m was required. The classical Nyquist equi-angular SNF data point spacing suggested the use of 1° in both θ- and ϕ-axes resulting in 32,400 points in all. The equivalent surface magnetic currents were then reconstructed using a 0.31λ by 0.31λ discretization yielding *circa* 9,000 unknowns in all, requiring *individual* complex arrays occupying ~64 GB of memory. Although this was processed using a modern desktop workstation, it did not require any specialist computing hardware, *e.g.* workstation clusters *etc*. Using the EC based CS processing algorithm presented above and in [7, 12, 13, 15] for this SNF case and assuming a simulated measurement noise level of -60 dB, the back projected *x*-polarised difference field on the non-canonical radome can be seen presented in Figure 4, and which accurately locates the position of the three defective regions on the radome surface. Here, three phase faults were introduced into the “defective” production test radome comprising 45° phase changes over a patch size of 8×8cm, or ~2.5×2.5 wavelengths at 9.3 GHz which are typical values based upon prior practical experience of radome measurements. Although the E_y and E_z fields are also obtained, these are not shown here due to the constraints of available space. Here, it is worth noting that for the commercial radome test case, the exact near amplitude and phase values are of lesser importance than is the *location* of any defect within the radome. Here, as has been done previously [7, 13, 15], the results were averaged over multiple sets, in this case three, with this being done to improve the recovery of the individual faulty patches. Here, 600 points per set of variable samples were used with the remaining 1,800 samples being fixed over the sets. This meant that the average number of CS points was 2,932 which corresponded to 13.4% of the number of samples required by a conventional equi-angular SNF acquisition. Figure 5a shows the azimuth cut for the true reference “gold”, blue trace, and true “defective”, red trace, radome cases when the weather radar has been mechanically scanned to boresight, *i.e.* azimuth = elevation = 0°.

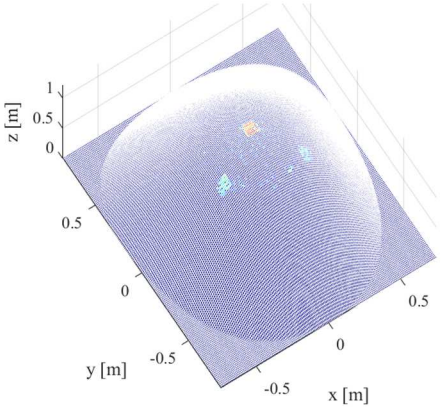

Figure 4: Difference E_x field between gold and defective radome on the radome surface showing correctly the location of the three faulty patches.

A measure of the adjacency of these two patterns is provided by the equivalent multipath level [14] which is represented here by the gold trace. Figure 5b contains an equivalent plot to that of Figure 5a, only here, the results were obtained from the CS based processing. Crucially, the agreement between the plots shown in Figures 5a and 5b attest to the excellent degree of success attained by the new CS processing, with even the very sensitive EMPL traces exhibiting the same form. This is further corroborated by the two-dimensional false-color checkerboard plots of the EMPLs shown in Figure 5c, and 5d, which provide a measure of the degree of agreement not just across a cardinal cut, but across all of the far-field pattern. Finally, if we compare the respective EMPL plots, we find that the True - CS recovered FF EMPL for an 80% CDF level was -57.8 dB. This can be seen presented in Figure 6 below.

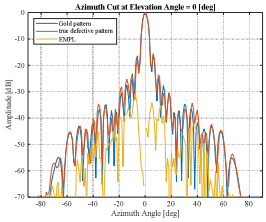

a) True azimuth plot of gold and defective radomes.

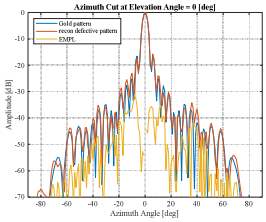

b) CS Reconstructed azimuth plot of gold and defective radomes.

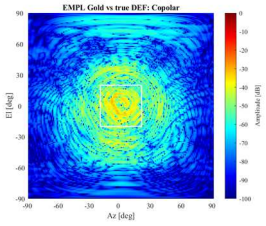

c) True Gold versus defective EMPL false colour plot.

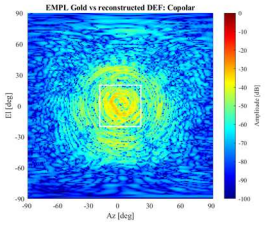

d) CS Reconstructed Gold versus defective EMPL false colour plot.

Figure 5: 737 Radome: Array Scanned to Boresight

Here, it is worth noting that although the agreement attained is very encouraging over the main beam and wide-out sidelobe region, the main-beam and first few sidelobes are of most interest with loss and beam deflection typically being of greatest concern and here, denoted by the white square, we can see EMPL levels of -40 dB or better.

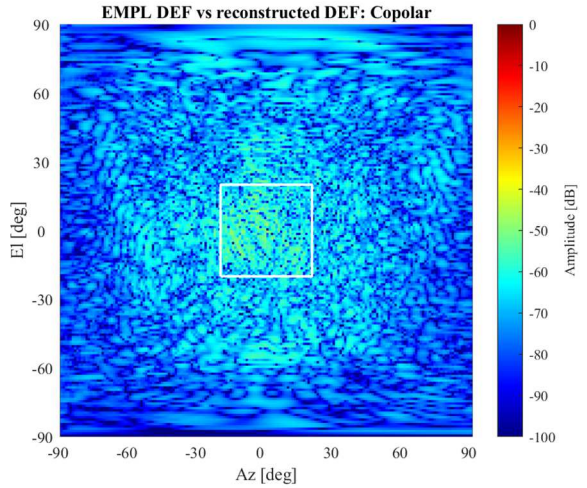

Figure 6: 737 Radome with array scanned to Az = 0°, El = 0°, showing EMPL plot comparing true defective to CS recovered defective.

By way of a further comparison, as DO-213A requires the weather radar to be mechanically scanned to a range of different pointing angles, Figure 7 contains equivalent results to those of Figure 5, only here the slotted waveguide antenna was scanned to Az =-25°, El = 0°. Again, excellent results can be seen. In this case, an average of 2,833 CS points were required which corresponded to 12.5% of a full conventional SNF acquisition.

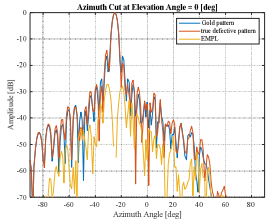

a) True azimuth plot of gold and defective radomes.

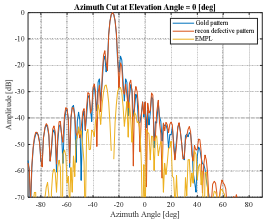

b) CS Reconstructed azimuth plot of gold and defective radomes.

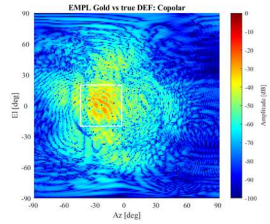

c) True Gold versus defective EMPL false colour plot.

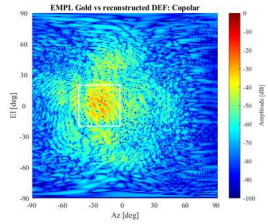

d) CS Reconstructed Gold versus defective EMPL false colour plot.

Figure 7: 737 Radome: Array Scanned to Az =-25°, El = 0°

Although only two examples have been shown here, it is important to note that in all, many thousands of test cases were examined with the weather radar being mechanically scanned over the full ±90° azimuth and ±25° elevation angular range specified by DO-213A with very similar results being obtained in each case.

IV. Radome Measurement Acceleration and Improved Imaging

As illustrated above, *cf.* Figure 4, the reconstruction of equivalent difference magnetic surface currents as a necessary step within the CS algorithm provides, for free and almost as a byproduct, the opportunity to image the production test radome. This is a valuable resource to engineers as it provides a great deal of information regarding the precise locations on a radome that may require further remedial attention. However, the sensitivity with which this information is recovered can depend upon the position of the fault and the angles to which the weather radar is scanned. The reason for this is that since the weather radar is a high gain aperture antenna, it is quite possible that when the radar antenna is pointed away from a fault that the field intensity with which that fault is illuminated can be greatly reduced when compared to the case when the radar is looking directly at the fault.

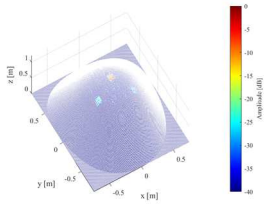

a) Scanned to Az = 0°, El = 0°

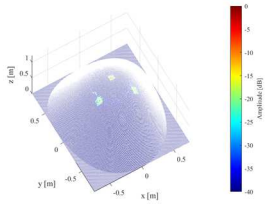

b) Scanned to Az = 0°, El =-25°

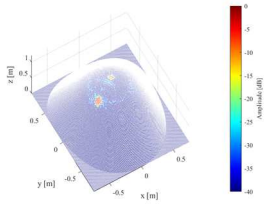

c) Scanned to Az = 0°, El =+25°

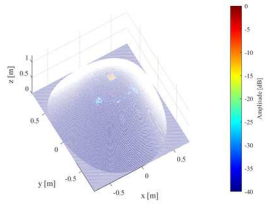

d) Scanned to Az =-25°, El = 0°

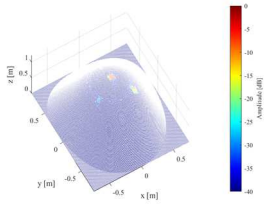

e) Scanned to Az = +25°, El = 0°

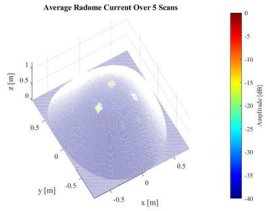

f) Result averaged over *five* individual measurements

Figure 8: 737 Radome: Surface current defects 'measured' using 5 different scans of the radar antenna, plus overall average

However, as the difference fields are related to the radome rather than to the mechanically scanning weather radar antenna, we are free to average the recovered difference fields to improve the signal to noise ratio and provide clearer images of the defects. An example of this can be seen presented in Figure 8 with the individual difference fields being shown in Figure 8a–8e, with the averaged difference field result being found in Figure 8f. Here, we can clearly see the improvement in the clarity of the reconstructed difference-field. While DO-213A requires the *unchanged* radome to be tested with the weather radar mechanically scanned to a large number of different positions, it does not specify the order that these measurements should be taken in. Thus, with no overall additional cost in terms of either time or effort, we may commence by measuring the radome with the antenna looking, for example: to the left, then to the right, then up, then down, and then finally straight ahead. This is in fact the set of measurements that are illustrated in Figure 8a – e. In this way, we stand a very good likelihood that we will detect at a very early stage in the radome measurement campaign whether there are significant defects in the test article. In the event that there are significant defects, the radome can be removed from the facility and sent for repair with a clear indication of where on the radome the defect is located freeing up valuable facility time. In all probability, this by and of itself may be one of the most significant cost savings. In the event that this initial test does not reveal any notable concerns, then the operator is free to continue the test campaign and complete the obligations dictated by the standard in the full knowledge that the test is worthwhile and that no time has been wasted.

V. Summary & Conclusions

Building on our previous work of formulating the EC total-difference based CS process for the case of SNF measurements of 'gold' and faulty scale model, commercial, nose-mounted radomes [7], we have applied the technique to the case of detecting the location of faults on a full-size Boeing 737 radome surface using SNF total-difference measurements of gold and 'faulty' production test radomes. Although the method does not allow of calibration of the exact amplitude and phase fault on the radome surface, the location of the fault is correctly identified and most importantly the defective SNF and corresponding FF radiation patterns are accurately reconstructed. Simulation results for a Boeing 737 radome have indicated that the CS method can recover the faulty radomes true FF radiation pattern to an EMPL of better than -56dB for 80% of the time using just ~13% of the full SNF sample set with this being verified statistically over many thousands of test cases, and has found to work in each and every case.

VI. References

[1] D.M. Lewis, J. Bommer, G.E. Hindman, S.F. Gregson, "Traditional to modern antenna test environments: The impact of robotics and computational electromagnetic simulation on modern antenna measurements," 15th European Conference on Antennas and Propagation (EuCAP), 2021

[2] D. Novotny, et al, "Performance evaluation of a robotically controlled millimeter-wave near-field pattern range at the NIST", 2013 7th European Conference on Antennas and Propagation

[3] J. Guerrieri, et al, "Configurable Robotic Millimeter-Wave Antenna Facility", 2015, 9th European Conference on Antennas and Propagation.

[4] J Guerrieri, et al, "Validation of Robotics for Antenna Measurements", 2017 11th European Conference on Antennas and Propagation.

[5] D. R. Novotny, J. A. Gordon, M. S. Allman, "The Multi-Robot Large Antenna Positioning System for Over- The-Air Testing at the National Institute of Standards and Technology", Proceedings of the AMTA Symposium.

[6] S.F. Gregson, D. Lewis, P. Schluper, G.E. Hindman, "Use of Model Based Systems Engineering and Development in the Design of a Commercial Nose-Radome Test System Employing a Multi-Axis Cobot", 2024, 17th European Conference on Antennas and Propagation, Glasgow, UK.

[7] S.F. Gregson, C.G. Parini, "Use of Compressive Sensing Techniques for the Rapid Production Test of Commercial Nose-Mounted Radomes in a Robotic Antenna Measurement System", EuCAP, 2025, Stockholm, Sweden.

[8] L. C. Potter, E. Ertin, J. T. Parker, and M. Cetin, "Sparsity and Compressed Sensing in Radar Imaging," Proc. IEEE, vol. 98, no. 6, pp. 1006–1020, 2010.

[9] M. Salucci, M. D. Migliore, P. Rocca, A. Polo and A. Massa, "Reliable antenna measurements in a near-field cylindrical setup with a sparsity promoting approach," IEEE Trans. Antennas Propag., vol. 68, no. 5, pp. 4143-4148, May 2020

[10] R. Cornelius, D. Heberling, N. Koep, A. Behboodi and R. Mathar, "Compressed sensing applied to spherical near-field to far-field transformation," in Proc. European Conf. Antennas Propag. (EuCAP), Davos, Switzerland, 2016, pp. 1-4.

[11] Z. Chen, S.F. Gregson, Y. Wang, "Novel Application of Compressed Sensing in Cylindrical Mode Filtering for Far-Field Antenna Measurements", Antenna Measurement Techniques Association Annual Symposium, October 2023, Seattle, USA.

[12] S.F. Gregson, Z. Qin, C.G. Parini, "Compressive Sensing in Massive MIMO Array Testing: A Practical Guide", IEEE Transactions on Antennas and Propagation, 2022, Volume: 70, Issue: 9.

[13] C.G. Parini, S.F. Gregson, "Compressive Sensing Applied to Planar Near-Field Based Array Antenna Diagnostics for Production Testing", AMTA 2023, October 2023, Seattle, USA.

[14] C.G. Parini, S.F. Gregson, J. McCormick, D. Janse van Rensburg, T. Eibert, "Theory and Practice of Modern Antenna Range Measurements 2nd Expanded Edition, Volume 1", IET Electromagnetic Waves series 55 ISBN 978-1-83953-126-2, 2021.

[15] C.G. Parini, S.F. Gregson "Recent Advances in Compressive Sensing for Production Test and Antenna Diagnostics of 5G Massive MIMO Antennas", 46th Annual AMTA Symposium, October 2024, Cincinnati, Kentucky, USA.

[16] RTCA SC-173, "Change No. 1 to RTCA/DO-213 Minimum Operational Performance Standards For Nose-Mounted Radomes" RTCA, Inc., www.rtca.org, 1995.

[17] RTCA SC-230, "RTCA/DO-220A, Minimum Operational Performance Standards (MOPS) for Airborne Weather Radar Systems", RTCA, Inc., www.rtca.org, 2016.

[18] RTCA SC-230, "RTCA/DO-213A Minimum Operational Performance Standards for Nose-Mounted Radomes," RTCA, Inc., www.rtca.org, 2016.

[19] R. Moch, D. Heberling, "Fast spline-based antenna measurements for robotic test ranges via pointwise probe correction," in Proceedings of the 16th EuCAP, 2022.

[20] M. P. Friedlander, E. van den Berg, "SPGL1: A Solver for Sparse Least Squares," 2007. [Online]. Available: http://www.cs.ubc.ca/labs/scl/spgl1

[21] Y. Zhang, W. Deng, J. Yang, W. Yin, "YALL1: Your Algorithms for L1," 2011. [Online]. Available: https://yall1.blogs.rice.edu/